applied optics

Hybrid spatial–temporal Mueller matrix imaging spectropolarimeter for high throughput plant phenotyping

Michael W. Kudenov,[1,*] Danny Krafft,[1] Clifton G. Scarboro,[1] Colleen J. Doherty,[2] and Peter Balint-Kurti[3,4]

[1]Electrical and Comprehensive Engineering and NC Plant Sciences Initiative, North Carolina State University, 840 Oval Drive, Raleigh, North Carolina 27695, USA
[2]Molecular and Structural Biochemistry, North Carolina State University, 128 Polk Hall, Raleigh, North Carolina 27695, USA
[3]Plant Science Research Unit, USDA-ARS, Raleigh, North Carolina 27606, USA
[4]Department of Entomology and Plant Pathology, North Carolina State University, Raleigh, North Carolina 27695, USA
*mwkudeno@ncsu.edu

Received 19 December 2022; revised 4 February 2023; accepted 5 February 2023; posted 6 February 2023; published 7 March 2023

Many correlations exist between spectral reflectance or transmission with various phenotypic responses from plants. Of interest to us are metabolic characteristics, namely, how the various polarimetric components of plants may correlate to underlying environmental, metabolic, and genotypic differences among different varieties within a given species, as conducted during large field experimental trials. In this paper, we overview a portable Mueller matrix imaging spectropolarimeter, optimized for field use, by combining a temporal and spatial modulation scheme. Key aspects of the design include minimizing the measurement time while maximizing the signal-to-noise ratio by mitigating systematic error. This was achieved while maintaining an imaging capability across multiple measurement wavelengths, spanning the blue to near-infrared spectral region (405–730 nm). To this end, we present our optimization procedure, simulations, and calibration methods. Validation results, which were taken in redundant and non-redundant measurement configurations, indicated that the polarimeter provides average absolute errors of $(5.3 \pm 2.2) \times 10^{-3}$ and $(7.1 \pm 3.1) \times 10^{-3}$, respectively. Finally, we provide preliminary field data (depolarization, retardance, and diattenuation) to establish baselines of barren and non-barren *Zea maize* hybrids (G90 variety), as captured from various leaf and canopy positions during our summer 2022 field experiments. Results indicate that subtle variations in retardance and diattenuation versus leaf canopy position may be present before they are clearly visible in the spectral transmission.

https://doi.org/10.1364/AO.483870

1. INTRODUCTION

Imaging Mueller matrix polarimetry (MMP) has been used in applications spanning biomedical imaging [1–4], industrial inspection [5,6], and optical testing [7]. For instance, in histological imaging, the use of MMP enables depolarization, retardance, and diattenuation to serve as label-free makers, enhancing the contrast of tissues for, e.g., identifying carcinoma during biopsies [4,8]. Yet, despite its more abundant use in biomedical imaging applications, the use of MMP to study plants and, in general, agricultural plant systems, is comparatively limited [9–12] compared to spectroscopy and fluorescence [13–16]. Fortunately, recent studies have highlighted polarimetry's utility in plant systems research as applied to early plant disease detection [17] and for contrast enhancement of structures within plant tissues [18]. For instance, Eeckhout *et al.* demonstrated that an imaging MMP can be used to better identify secondary veins within leaves, when compared to regular intensity imaging [18]. An interesting attribute is that contrast is not necessarily maximized at one input polarization state, necessitating the use of a full MMP measurement to obtain optimal contrast. Similarly, Bugami *et al.* demonstrated that leaf tissue microscopy, using an imaging MMP, enabled oxalate raphides to be clearly identified in imagery, whereas unpolarized intensity imaging produced little to no discernible contrast of these structures [11].

While such studies are enlightening, there is also a general interest to acquire MMP data that span a larger number of samples, measured across many trials, treatments, and replicates in field conditions, which may have many forms or types of ground truth—beyond the tissue's structural components. Specifically, of equal interest are metabolic components. For example, starch granules show strong polarization dependencies that may be detectable in macroscopic measurements of plant leaves [19]. Having a more general association between polarization metrics

and how they may compliment other, more mature, means of plant measurements (e.g., spectroscopy and fluorescence) is therefore of key long-term interest. Thus, instrumentation that can enable the rapid collection of imaging MMP baselines would allow for down-stream comparison of these baselines to, e.g., nuclear magnetic resonance (NMR) spectroscopy, inductively coupled plasma mass spectrometry (ICP-MS), pigment assays, CO_2 assimilation rate, photosystem operating efficiency metrics, and carbohydrate content. Furthermore, how these baselines and associated metrics may depend on other treatments, such as abiotic and biotic stress, time of day, environmental conditions, plant variety, and ecology within field-scale experiments is also of interest for imaging MMP measurements.

To enable rapid measurements in the field to best support these use-cases, we optimized and built a transmission-mode Mueller matrix imaging polarimeter. Our goal was to measure leaf samples, with a high spatial resolution (2.5 μm), across 10 spectral bands within approximately 30 s. This high spatial and temporal resolution was achievable by the use of: (1) LEDs to electrically and rapidly switch between the different spectral bands; (2) fast piezo-driven rotation stages for temporal modulation; and (3) a microgrid focal plane imaging camera [20,21], by which fewer overall images needed to be collected to form a single Mueller matrix measurement at each wavelength. In addition to fulfilling the application's needs, this imaging MMP design represents a complex tradespace and testbed to which emerging tools and optimization strategies can be applied, as per Alenin and Tyo [22,23] using channeled polarimeter techniques [24–28]. However, in our study, we apply the conventional eigenvalue calibration method for optimization, calibration, fitting, and characterization of the polarimeter [10,29,30], with the expectation of using the instrument as a testbed to further explore, e.g., maximum likelihood calibration [31] and generalized channeled polarimeter calibration and optimization techniques [22].

This paper is organized as follows: Section 2 illustrates the system layout, Section 3 describes aspects of the illuminator's design and simulation, Section 4 overviews the experimental setup, Section 5 describes the calibration and modeling, Section 6 provides results taken with the system in both the laboratory on validation targets and outdoors of a *Z. maize* hybrid, Section 7 provides a discussion, and Section 8 provides a conclusion.

2. SYSTEM LAYOUT

The sensor concept leverages a hybrid modulation scheme [22], where temporal modulation is offered by two rotating achromatic quarter-wave plates (QWPs), and spatial modulation is provided by a commercially available microgrid polarization camera. The sensor's design is illustrated in Fig. 1. Light from several single-color light-emitting diodes (LEDs) is coupled into an integrating rod (I-Rod) using individual polymer optical fibers. After the light is homogenized by the I-Rod, the light is relayed onto the sample using a condenser lens C1, after which it becomes linearly polarized at 0° by a linear polarizer (LP). A rotating achromatic QWP (QWP_G) in the polarization state generator (PSG) is positioned upstream of an isotropic glass window (W1). After transmitting through the sample, light

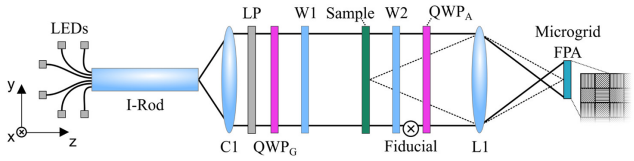

Fig. 1. System schematic of the Mueller matrix imaging polarimeter. LEDs, light-emitting diodes; LP, linear polarizer; C1, condensing lens; W1, W2, windows; QWP_G, QWP_A, quarter-wave plates; L1, lens; FPA, focal plane array; I-Rod, integrating rod.

transmits through a second isotropic glass window (W2) before passing through a second rotating achromatic QWP (QWP_A) in the polarization state analyzer (PSA). Sample light is imaged by lens L1 onto a polarized microgrid focal plane array (FPA), which contains the LPs, within each superpixel, which serves as the PSA's final component. Finally, a horizontally oriented fiducial surface exists, as part of the sensor's housing, behind window W2. As will be discussed in Section 5, this was used as a reference surface to validate known polarization elements, and was necessary due to the small sample compartment size of the final system.

3. SIMULATIONS

Simulations were conducted to: (1) optimize the orientations of QWP_G and QWP_A to maximize performance with the minimum number of measurements; and (2) design the illumination system to achieve uniform sample irradiance.

A. Optimization

Mueller calculus was used to model the sensor's polarization elements [32]. A diattenuator's Mueller matrix can be expressed as

$$\mathbf{M}_D(T_x, T_y, \theta_D) = \frac{1}{2}\mathbf{R}(-\theta_D)\begin{bmatrix} 1 & D & 0 & 0 \\ D & 1 & 0 & 0 \\ 0 & 0 & 2E & 0 \\ 0 & 0 & 0 & 2E \end{bmatrix}\mathbf{R}(\theta_D), \quad (1)$$

where θ_D is the transmission axis orientation, $\mathbf{R}$ is the rotation matrix, D is the diattenuation

$$D = \frac{(T_x - T_y)}{(T_x + T_y)}, \quad (2)$$

$$E = \frac{\sqrt{T_x T_y}}{(T_x + T_y)}, \quad (3)$$

and T_x and T_y are the x- and y-axis transmission coefficients, respectively. The rotation matrix can be expressed as

$$\mathbf{R}(\theta) = \begin{bmatrix} 1 & 0 & 0 & 0 \\ 0 & \cos(2\theta) & \sin(2\theta) & 0 \\ 0 & -\sin(2\theta) & \cos(2\theta) & 0 \\ 0 & 0 & 0 & 1 \end{bmatrix}. \quad (4)$$

Finally, a retarder's Mueller matrix can be expressed as

$$\mathbf{M}_R(\delta, \theta_r) = \mathbf{R}(-\theta_r)\begin{bmatrix} 1 & 0 & 0 & 0 \\ 0 & 1 & 0 & 0 \\ 0 & 0 & \cos\delta & \sin\delta \\ 0 & 0 & -\sin\delta & \cos\delta \end{bmatrix}\mathbf{R}(\theta_r), \quad (5)$$

where δ is the retardance, and θ_r is the retarder's fast axis orientation.

The camera's superpixels contain $N_{SP} = 4$ LPs with transmission axis orientations of 0°, 45°, 90°, and 135° [33]. The Mueller matrix of each pixel n within the superpixel can be calculated by

$$\mathbf{M}_{nij} = \mathbf{M}_D\left(T_{xn}, T_{yn}, \theta_n\right)\mathbf{M}_R\left(\delta_{L1}, \theta_{L1}\right)\mathbf{M}_R(\delta_A, \theta_A) \times \mathbf{M}_S\mathbf{M}_R(\delta_G, \theta_G)\mathbf{M}_D\left(T_{xG}, T_{yG}, \theta_{\mathrm{LP}}\right), \quad (6)$$

where θ_n, T_{xn}, and T_{yn} are the pixels' diattenuator's coefficients per Eq. (2); T_{xG} and T_{yG} are the generating polarizer's x and y transmission coefficients, δ_G and θ_G are the generator QWP's retardance and fast axis orientation, and δ_A and θ_A are the analyzer QWP's retardance and fast axis orientation, respectively; $\mathbf{M_S}$ is the sample's Mueller matrix; δ_{L1} and θ_{L1} are polarization aberration parameters that account for the objective lens's stress birefringence; and i and j are integers denoting the x and y coordinates of a superpixel on the 2D array, respectively. The intensity of each pixel can be calculated by

$$I_n(i, j) = \begin{bmatrix} r_n(\lambda) & 0 & 0 & 0 \end{bmatrix}\mathbf{M}_{n,i,j}\mathbf{S}_{in}, \quad (7)$$

where r_n is the relative responsivity of the nth pixel, and all of the parameters in Eqs. (6) and (7) have a spatial dependence i and j.

First, calculations were performed to identify the optimal choices of fast axis orientations, assuming that $\mathrm{QWP_G}$ and $\mathrm{QWP_A}$ had ideal retardance. Optimization consisted of the following.

1. Synthesizing $N_S = 5000$ randomly generated sample Mueller matrices, formed by
$$\mathbf{M}_S = \mathbf{M}_D(T_{x\rho}, T_{y\rho}, \phi_{D\rho})\mathbf{M}_R(\delta_\rho, \phi_{R\rho}), \quad (8)$$
where uniform random variables for the diattenuator's transmittances $T_{x\rho}$ and $T_{y\rho}$ span zero to one, orientations of the diattenuator and retarder $\phi_{D\rho}$ and $\phi_{R\rho}$, respectively, span 0°–360° (though 0°–180° is sufficient), and the retarder's retardance $\phi_{R\rho}$ spans 0°–360°.
2. Software (*MATLAB R2021a*) was used to randomly select the $\mathrm{QWP_G}$ and $\mathrm{QWP_A}$ orientations by assigning θ_G and θ_A values from a uniform distribution spanning 0°–180°. For the purposes of this simulation, $\delta_A = \delta_G = 90°$ due to the achromatic QWPs (Bolder Vision AQWP3). Since we wanted to minimize the measurement time, we constrained the number of generator orientations to two and the number of analyzer orientations to four, the minimum required to solve all 16 elements of the Mueller matrix using this system, given that the microgrid contains only LPs.
3. A Monte Carlo simulation was performed in which the random variables θ_G and θ_A in #2 were generated $N_c = 20000$ times.
   (a) For each configuration, Eq. (6) was used to calculate each pixel's Mueller matrix. For each of the eight randomly selected orientations (two for the generator and four for the analyzer, yielding a total of eight camera images) a 32×16 element measurement matrix $\mathbf{W}$ was assembled for the superpixel [32].
   (b) For each sample Mueller matrix $\mathbf{M_S}$, the signal intensity was simulated using $\mathbf{W}$ by
   $$\mathbf{I_n} = \mathbf{W}\mathbf{M}_S + \mathbf{n}, \quad (9)$$
   where $\mathbf{I}$ is a 32×1 vector of simulated pixel intensities, and $\mathbf{n}$ is a 32×1 vector of Poission distributed shot noise. Noise was simulated by normalizing $\mathbf{I_n}$ to its maximum value before scaling it to a maximum photon count of 2500, yielding a maximum signal-to-noise ratio (SNR) of 50 in each vector $\mathbf{I_n}$.
   (c) The Mueller matrix elements were then calculated from $\mathbf{I_n}$ by
   $$\mathbf{M}'_{\mathrm{RS}} = \mathbf{W}^{-1}\mathbf{I_n}, \quad (10)$$
   where $\mathbf{W}^{-1}$ was calculated by its pseudo inverse.
   (d) The mean squared error (MSE) was then calculated by comparing the simulated Mueller matrix elements $\mathbf{M}'_{\mathrm{RS}}$ from Eq. (10) to the input $\mathbf{M_{RS}}$. The optimal orientations were then selected based on the minimum MSE.

It was determined that one set of nearly optimal values included $\theta_G = [22.5°, 67.5°]$ and $\theta_A = [10°, 53°, 121°, 165°]$. Notable are that generator orientations of $\theta_G = [45°, 90°]$ performed similarly to those selected here for these values of θ_A. This is observed more clearly when the MSE was calculated for θ_A fixed at [10°, 53°, 121°, 165°] for arbitrary $\theta_G = [\theta_1, \theta_2]$ per Fig. 2(a). From these data, a band of minimum MSE exists for generator QWP orientations that are separated by $|\theta_1 - \theta_2| = 45°$. Similarly, there is a wide selection of generator orientations that perform well for fixed generator fast axis orientations of $\theta_G = [22.5°, 67.5°]$ for select values $\theta_A = [\theta_a, \theta_b, \theta_c, \theta_d]$. These results are depicted in Figs. 2(b)–2(f) assuming a fixed $\theta_a = 10°$ for θ_b equal to 0°, 25°, 53°, 75°, and 100°. Of these analyses, our optimal solutions of θ_c and θ_d are presented in Fig. 2(d), which highlights the region containing $\theta_c = 121°$ and $\theta_d = 165°$. While these figures illustrate only a small and arbitrary subset of the many possible visualizations that could be produced of this multidimensional optimization space, it illustrates that the chosen point is but one of several minima that exist (many minima are generally -22 ± 0.5 dB). Thus, other combinations of $\theta_A = [\theta_a, \theta_b, \theta_c, \theta_d]$ may offer equivalent performance. Whether other performance metrics, such as the condition number, Frobenius norm, equally weighted variance [34], etc., impact performance for specific matrices is of interest for future studies.

B. Optical Design of the Illumination System

Simulations were performed in Zemax to design the illumination system. A key focus of the design was to minimize the required measurement time, for highly absorbing samples, to increase measurement throughput. We tested several illumination sources in the laboratory to ensure sufficient radiometric throughput after transmitting through whole and in-tact maize leaves. Our prior experiments [10] were performed using a xenon arc lamp coupled into a monochromator with a spectral bandwidth of approximately 5 nm. Using this setup, we configured our existing Mueller matrix imaging polarimeter

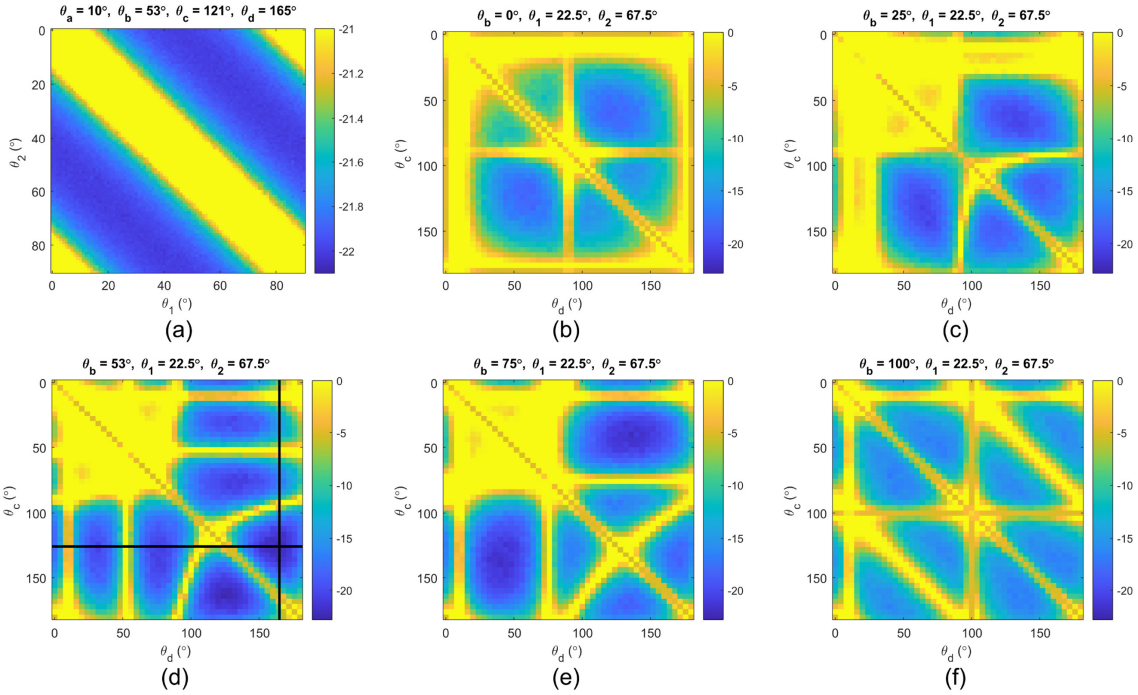

Fig. 2. MSE, in dB, versus angle for specific combinations of $\theta_G = [\theta_1, \theta_2]$ and $\theta_A = [\theta_a, \theta_b, \theta_c, \theta_d]$. (a) $\theta_G = [\theta_1, \theta_2]$ for $\theta_A = [10°, 53°, 121°, 165°]$; (b)–(f) changes in θ_c and θ_d for fixed $\theta_G = [22.5°, 67.5°]$ and $\theta_a = 10°$, including (b) $\theta_b = 0°$, (c) $\theta_b = 25°$, (d) $\theta_b = 53°$, (e) $\theta_b = 75°$, and (f) $\theta_b = 100°$. Black lines in (d) indicate our optimal minimum error.

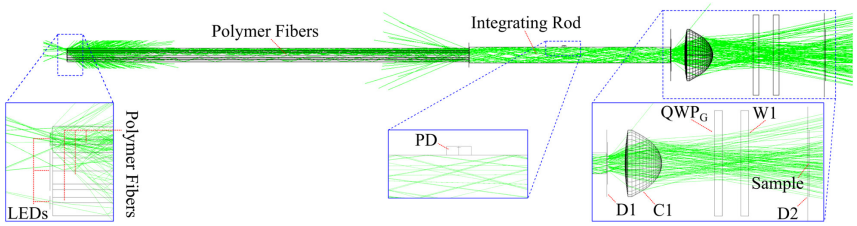

Fig. 3. Zemax simulation layout of the LED illuminator. PD, photodiode; D1, D2, simulated 2D detectors; C1, collimator lens; QWP_G, quarter-wave plate; W1, window.

[5] using the same monochromator, liquid light guide, and arc lamp [10].

A corn leaf was used to establish an optimal integration time at a 680 nm wavelength using the arc lamp. Different light sources were then compared to each other using the same monochromator and liquid light guide to ensure equivalent radiometric performance. A 1 W monochromatic high powered LED, with a center wavelength of 680 nm, and a 35 W tungsten halogen lamp (direct current, 12 V) were then tested. This test indicated that an integration time similar to that obtained with the arc lamp could be achieved using the high powered LED, whereas the camera's integration time, when using the tungsten–halogen lamp, was an order of magnitude greater. Note that lasers were not tested due to the difficulty in reducing speckle noise and the overall complexity (size, weight, power) of solutions needed to reduce speckle noise throughout the measurement cycle [35,36].

Since LEDs provided the best performance, we designed an illuminator using polymer-fiber coupled LEDs. This enabled most of the LED's energy to be directed into an I-Rod within a compact area, without the need to create custom-tailored printed circuit boards with individually addressable LED connections. This also offers the capability to rapidly replace, upgrade, or change LEDs at a later time if needs change. A view of the Zemax simulation is provided in Fig. 3. Light from the LEDs was modeled as a Lambertian surface closely positioned to the end of the fiber. To model a numerical aperture (NA) of 0.6, each fiber was modeled as a rod with a refractive index of 1.18 in air. Each fiber end was then placed in close proximity to the I-Rod's entrance face, which was modeled as an $8 \times 8 \times 100$ mm^3 N-BK7 glass rectangular volume.

An aspheric condenser lens, with a focal length of 16 mm, was then placed at the I-Rod's exit face. This lens collimated the light from the rod's exit face through the generator QWP (QWP_G) and window (W1), which were modeled in the system to ascertain backreflections. Finally, a photodiode (PD) was also modeled as being index coupled to the I-Rod. This enabled the signal to be simulated to determine whether a PD sensor in this location could effectively monitor the LEDs' stability over time during the course of regular measurements. Simulated detectors, D1 and D2, were used to quantify the radiometric output and uniformity of the sample planes. A view of the detector

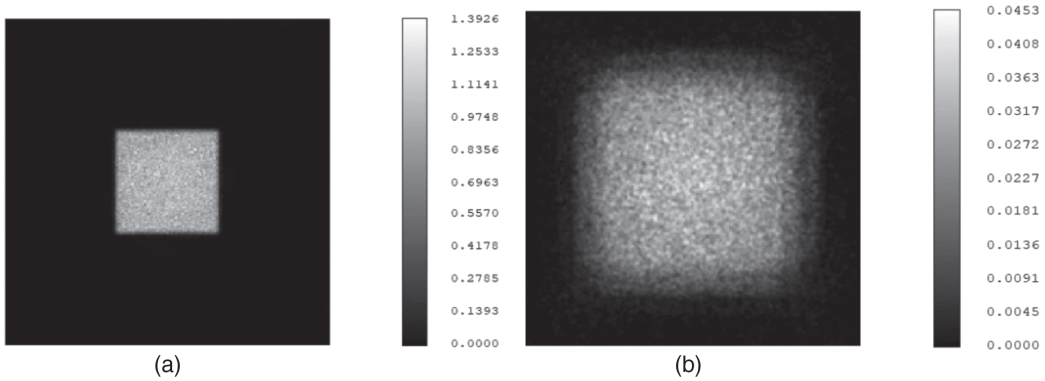

Fig. 4. (a), (b) Detector output from detectors D1 and D2, respectively. Colorbar units are irradiance in W/cm^2.

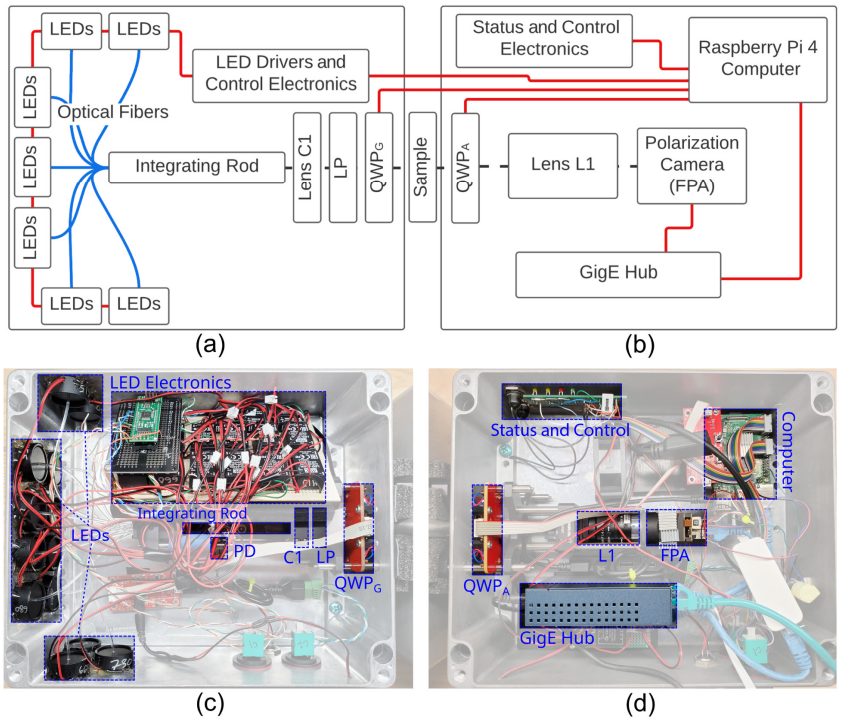

Fig. 5. Schematics and photos of the system on the benchtop. (a), (c) Polarization state generator with illumination LEDs and LED drivers; and (b), (d) polarization state analyzer with camera and control electronics.

output is depicted in Fig. 4. The total power simulated at the LED was 1 W, of which 0.366 W was directed to detector D1 [the rod's output face, Fig. 4(a)], and 0.268 W was coupled into detector D2 [the sample, Fig. 4(b)]. Overall, this represents approximately 26.8% coupling efficiency.

4. EXPERIMENTAL SETUP

After optimizing the wave plate orientations and designing the illuminator, we set up the system in the laboratory to create a ruggedized sensor that could withstand wind-driven rain and severe weather events for prolonged periods of time. As such, all components were housed within two IP67-rated aluminum enclosures. Non-anodized aluminum was selected to minimize the risk of sensor overheating in direct sunlight. Two enclosures were used: one for the generator's components and one for the analyzer's components.

A schematic and photo of the sensor's generator are depicted in Figs. 5(a) and 5(c), respectively. It consists of high powered LEDs, mounted on star-shaped printed circuit boards, with wavelengths of 405, 415, 455, 530, 615, 660, 680, 700, 730, and 850 nm. These LEDs are mounted directly to the aluminum enclosure's sidewall using thermally conductive epoxy and do not require additional cooling or heatsinking. LEDs were controlled using a microcontroller (68HC12) and powered by LED constant-current driver chips (Mean Well LDD-1500, −1000, −600, and −500) of appropriate capacity for the given LED. The I-Rod connects to the incoming polymer optical fibers (2 mm diameter core) using a 3D printed part into which all of the optical fibers can be secured to the rod's face. The PD (LTR-303ALS-01) is index matched to the rod using optical epoxy, which enables efficient coupling, to measure the LED's relative optical output power throughout the course of each sampling sequence. An aspheric collimation lens C1

(Thorlabs ACL25416U-A) couples the rod's light into a free-standing LP [Bolder Vision UHC with visible anti-reflection (AR) coatings], while a piezoelectric rotation mount (Thorlabs Elliptic series) serves to rotate the generating QWP (Bolder Vision free-standing AQWP3 with visible AR coatings).

A schematic and photo of the sensor's analyzer and computer control components are depicted in Figs. 5(b) and 5(d), respectively. Optics included the analyzing QWP (Bolder Vision AQWP3), an imaging lens L1 (Navitar 25 mm focal length, F/1.4), and a gigabit ethernet (GigE) polarized microgrid FPA (Lucid Vision Labs Phoenix PHX050S1-PC-FFC). A Raspberry Pi 4 (ARM64 architecture), running Ubuntu 20.04 server and using a custom kernel that enabled jumbo packets, operated the camera using the manufacturer's software development kit. A GigE network hub provided the ability for the sensor to be connected to a wireless module for remote administration of the Raspberry Pi 4 in the field, as well as dedicated computers for debugging, aligning, and focusing the camera in the laboratory. Finally, status LEDs and control buttons provided feedback and control, respectively, while using the scanner in the field.

A few other design considerations included: (1) free-standing (non-laminated) wave plates were used to minimize the stage's load, maximize rotational speed and lifespan, and minimize image translation; (2) the 850 nm wavelength was not intended for polarimetry due to the reduced performance of the generating LP for wavelengths longer than 750 nm; and (3) the sensor's weight is approximately 7 kg—a weight that could easily be reduced for future iterations of the scanner, but for now makes it challenging to use without a tripod in the field.

5. CALIBRATION

Calibration consisted of fitting Eq. (7) to data measured with an empty polarimeter. To maximize redundancy during characterization, calibration data were collected using a more conventional 26-measurement procedure (as opposed to the hybrid eight-measurement procedure highlighted in Section 3.A). During calibration, the generating QWP was rotated from 0° to 180° in 7° increments. The analyzer was then rotated in 35° increments to maintain a rotation ratio of 5:1 between θ_A:θ_G. Model fitting was then performed across all of the camera's four polarization channels, depicted for a microgrid polarization camera in Fig. 6(a). The intensity from all four channels was assembled into a 104×1 element vector before fitting, as depicted in Fig. 6(b). Finally, for the purposes of our calibration, we assumed that the parameters were spatially uniform across the field of view (FOV). This was based on the objective lens's (L1) relatively long focal length ($f = 25$ mm) and its use at higher focal ratios (in our case, F/4), which reduces polarization aberrations [37]. The off-axis portions of the FOV were further restricted by vignetting, such that only the inner 80% of the FOV was used.

During fitting, fixed *a priori* parameters substituted into Eq. (6) included

$$T_{xG} = 1 \tag{11}$$

$$T_{yG} = \frac{1}{h_G(\lambda)}, \tag{12}$$

where h_G is the polymer LP's extinction ratio provided by the manufacturer. Typical values of the polarizer's extinction ratio included 155 at 405 nm, 3400 at 530 nm, 1763 at 680 nm, and 543 at 700 nm. Additionally, the parameters related to the individual pixels' responsivity, $r_n(\lambda)$ in Eq. (7), were measured at each of the LED's center wavelengths by imaging the exit port of a 100 mm diameter integrating sphere, illuminated by a monochromator (Horiba Micro HR140) and xenon arc lamp (Optical Building Blocks XBO75). Finally, the camera's pixellated LPs' extinction ratios, $h_A(\lambda)$, were obtained from the manufacturer, such that $T_{xn} = 1$ and $T_{yn} = 1/h_A(\lambda)$. Some specific values of h_A obtained from the datasheet included 350 at 405 nm, 340 at 530 nm, 100 at 680 nm, and 95 at 700 nm. The camera's microgrid LP transmission axes θ_N were also assumed to be fixed during fitting at 0°, 45°, 90°, and 135°.

Other model parameters were fitted using *MATLAB R2021a* and a bounded fminsearch function [38]. Parameters for the generator and analyzer QWP and LP were fit such that

$$\theta_A = \theta'_A + \epsilon_A, \tag{13}$$

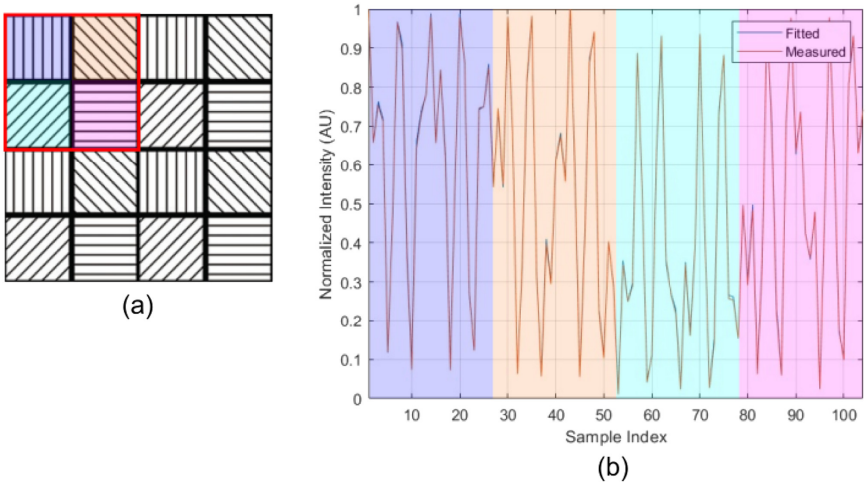

Fig. 6. 26-measurement calibration procedure. (a) The measured intensity was extracted from each of the camera's four polarization channels, and (b) fitting was performed across all four channels simultaneously.

Table 1. Summary of Fixed and Variable Parameters Used During Calibration

Description	Parameter	Degree of Freedom
QWP_A retardance	δ_A	δ_A
QWP_G retardance	δ_G	δ_G
Lens L1 retardance	δ_{L1}	δ_{L1}
Lens L1 retardance orientation	θ_{L1}	θ_{L1}
QWP_A fast axis angle	$\theta_A = \theta'_A + \epsilon_A$	ϵ_A
QWP_G fast axis angle	$\theta_G = \theta'_G + \epsilon_G$	ϵ_G
LP transmission axis	$\theta_{LP} = \theta'_{LP} + \epsilon_{LP}$	ϵ_{LP}
Microgrid orientation	$\theta_n\|_{n=1,2,3,4}$	Fixed (0°,45°,90°,135°)
Microgrid transmittance (x)	$T_{xn}\|_{n=1,2,3,4}$	Fixed (1.0)
Microgrid transmittance (y)	$T_{yn}\|_{n=1,2,3,4}$	Fixed ($1/h_A(\lambda)$)
Microgrid responsivity ($n = 1$)	r_1	Fixed
Microgrid responsivity ($n = 2, 3, 4$)	r_2, r_3, r_4	r_2, r_3, r_4

$$\theta_G = \theta'_G + \epsilon_G, \text{ and} \tag{14}$$

$$\theta_{LP} = \theta'_{LP} + \epsilon_{LP}, \tag{15}$$

where ϵ_A, ϵ_G, and ϵ_{LP} are variables available for fitting, θ'_A and θ'_G are the analyzer's and generator's nominal fast axis orientations, respectively, and θ'_{LP} is the LP's nominal value of 0°. Conversely, δ_A and δ_G were fit directly assuming nominal starting values of 90°, and the lens's retardance parameters, δ_{L1} and θ_{L1}, were fit directly assuming initial values of 0°. Finally, after images had their pixel responsivities corrected with the previously measured values of r_n, a degree of freedom for the responsivity of r_2, r_3, and r_4 was included with a fixed r_1, to reduce the impact of scaling errors between individual channels. A summary of the variables used in the calibration are detailed in Table 1.

A. Calibration Targets

Due to the instrument's relatively narrow sample chamber, it was not possible to verify the calibration against typical standards, such as the diattenuation caused by a steeply tilted single-surface Fresnel reflection, retardance caused by total internal reflection, or a rotating LP [5]. Consequently, two square-aperture, AR coated, free-standing LPs (BVO UHC) were prepared, such that their transmission axes were nominally oriented at 0° ± 1° [Fig. 7(a)] or 45° ± 1° [Fig. 7(b)] when a reference edge, parallel to the films' x axes, was placed against a fiducial located inside the instrument per Fig. 1. As also highlighted in Figs. 7(a) and 7(b), use of a square aperture also enabled measurements of polarizers at 90° ± 1° and 135° ± 1° by defining a second reference edge parallel to the films' y axes. Each polarizer contained two stacked films, which increased the extinction ratio to reduce the impact of the polymer polarization films' retardance during validation.

Additionally, two polymer wave plate films, a half-wave plate (HWP) and QWP, were cut with their fast axes nominally oriented at 45° ± 1° [Fig. 7(c)] and 35° ± 1° [Fig. 7(d)], respectively, the films' x axes. The films had optical path differences of 280 nm at $\lambda = 560$ nm and 165 nm at $\lambda = 680$ nm. Similar to the polarizers, a reference edge was also defined along the films' y axes to enable fast axis orientations of either 135° ± 1° or 125° ± 1° to be measured as per Figs. 7(c) and 7(d), respectively. Finally, all samples (polarizers and wave plates) were characterized and measured in their "flipped" orientation, in which films were rotated by 180° in the xz or yz planes. This provided a total of four orientations and measurements per film.

For elements made with a single (non-stacked) film, the fast axis angle in the flipped orientation should follow

$$\theta_{\text{flipped}} = [180° - \theta_{\text{nominal}}] \pm \epsilon_\theta, \tag{16}$$

where ϵ_θ is the positional repeatability error against the fiducial (measurements of this error are discussed in Section 6.B). While the repeatability error is valid for all targets, it should be noted that the relationship of Eq. (16) is valid only for the wave plate films [Figs. 7(c) and 7(d)]. Since these films were cut from a single layer, the fast axis orientation in both nominal and flipped orientations is not independent. This independence is not present for the LPs [Figs. 7(a) and 7(b)] since these used two films to obtain higher extinction.

As an added calibration target, Fresnel reflection was measured, in transmission, from a tilted 1 mm thick UV fused silica microscope slide placed inside the sample space. The slide was tilted to provide an incidence angle of 30.7° with respect to the slide's surface normal. Due to the aforementioned space limitations, the rotation was limited to the xz plane per Fig. 1. For single-pass transmission, we modeled this as a diattenuator

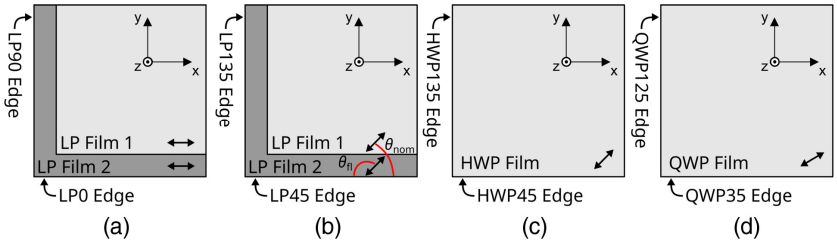

Fig. 7. Reference polarizers and wave plates used for calibration. Linear polarizers consisted of films with transmission axes at (a) 0° and 90° and (b) 45° and 135°. Single sheets of polymer retardation films were also created using a (c) 280 nm optical path difference sheet (nominally half-wave at a 560 nm wavelength) with a fast axis at 45° or 135° and (d) 165 nm optical path difference sheet (nominally quarter-wave at a 660 nm wavelength) with a fast axis at 35° or 125°. Transmission or fast axes were oriented at θ_{nom} or θ_{fl} with respect to each reference edge, which is only shown in (a) for clarity.

based on the Fresnel equations and the refractive index of fused silica [5,39].

B. Calibration Target Characterization

LPs were measured using the system depicted in Fig. 8(a) in which light from a white LED source was collimated by lens C through the reference polarizer $\mathbf{M}_{\mathrm{LPR}}$, which represents the Mueller matrix of the reference polarizers in Figs. 7(a) and 7(b). A rotating LP LP(θ) was positioned in front of a lens L and detector D. The transmission axis of each film, in either its nominal ("nom") or flipped ("fl") orientation, against each reference edge, was measured by the following.

1. Establishing a relative reference between the external polarizer, LP(θ), and one of the reference polarizers. The LP0 nominal position was selected per Fig. 8(b) to align the rotating polarizer LP(θ) such that it nominally blocked the light reaching the detector D.
2. Each polarizer's reference edge was then placed sequentially against the fiducial surface, and LP(θ) was rotated to extinguish the transmitted light. Since the transmission axis orientation of the two polarizers that form the "stack" can be different, the blocking orientation θ was recorded for both nominal and flipped positions.

This procedure had an estimated accuracy of $\pm 0.5°$ and was used to establish that the polarizers had been cut from the original film and aligned to one another to within $\pm 1°$. From these measurements, the polarizer's transmission axes were measured as provided in Table 2, which indicates that the transmission axis orientations are within the expected tolerances for both orientations.

Measurements were also made of the QWP and HWP. To simplify characterization, measurements were made only to quantify the films' retardance at each LED. Uncertainty in the fast axis orientations were mitigated by taking measurements in both nominal and flipped orientations as per Eq. (16).

The films' retardance was measured using the system depicted in Fig. 8(b). To mitigate error related to the LED's broader spectral bandwidth versus that of a monochromator, light from the system was coupled into a collimating lens (C) using an optical fiber, which was index matched to the I-Rod using glycerin. The rotating wave plate under test, $\mathbf{M}_{\mathrm{WPR}}(\theta)$, was placed between two parallel LPs with transmission axes at 0°. An objective lens (L) then focused light onto a detector (D). Each wave plate was rotated from 0° to 180° in 10° increments, and the detected intensity was fit to the system's Mueller matrix model. Tabular results of the LEDs' measured spectral full width at half maximum bandwidth ($\Delta\lambda$), HWP retardance (δ_{HWP}), and QWP retardance (δ_{QWP}) are provided in Table 3 for each LED wavelength. Additionally, the retardances' estimated errors, ϵ_{HWP} and ϵ_{QWP}, are also provided in Table 3. These errors were caused by discrepancies between the sensor's spectral response and that of the characterization setup, the retarder's dispersion, and the LED's spectral bandwidth. Typically, error increases when the retarder's dispersion, $d\delta/d\lambda$, is high and the LED's spectral bandwidth is large due to the greater degree of spectral uncertainty.

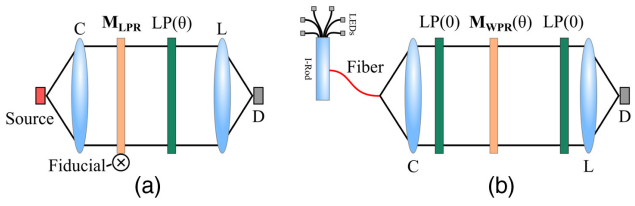

Fig. 8. Measurement configurations used to quantify (a) reference linear polarizers' transmission axis orientations and (b) reference wave plates' retardance versus wavelength.

Table 2. Measured Reference Polarizer (Pol.) Transmission Axis Angles (Ang.) Relative to the Nominal LP0 Position

	Pol.						
Ang.	**$\mathrm{LP0_{fl}}$**	**$\mathrm{LP90_{nom}}$**	**$\mathrm{LP90_{fl}}$**	**$\mathrm{LP45_{nom}}$**	**$\mathrm{LP45_{fl}}$**	**$\mathrm{LP135_{nom}}$**	**$\mathrm{LP135_{fl}}$**
θ	−1°	89°	90°	45°	136°	135°	45°

6. RESULTS

A. Reference Element Repeatability

First, the positional repeatability of the fast or transmission axis orientations was measured by placing the QWP into the system, in both its nominal and flipped orientations, four times, yielding eight total measurements. For each trial, the wave plate was physically removed and re-inserted against the sensor's fiducial. A theoretical Mueller matrix was defined, using the characterization data from Table 3 and the fast axis orientation per Section 5.A at each wavelength, and compared to the measured matrix. Error was calculated by

$$\boldsymbol{\epsilon}_{u,l}(\lambda_k) = \mathbf{M}_{\mathrm{meas},u,l}(\lambda_k) - \mathbf{R}(-\theta - \Delta\theta)\mathbf{M}_{\mathrm{theo},u,l}(\lambda_k)\mathbf{R}(\theta + \Delta\theta), \quad (17)$$

where $\Delta\theta$ is the fast axis error, k is an integer spanning 1 to $K = 9$ for each LED wavelength per Table 3, l is an integer spanning 1 to L that denotes each reference target, and u is an integer spanning 1 to U denoting each trial. The theoretical matrix's fast axis orientation was then adjusted using $\Delta\theta$ until the MSE, calculated using all 16 elements of $\boldsymbol{\epsilon}_{u,l}$, was minimized within each trial. From this procedure, the 2σ orientation repeatability error was measured to be $\epsilon_\theta = 1.1°$. To better isolate positional repeatability errors from that of the underlying polarimeter's error, we performed a similar optimization procedure during characterization by implementing Eq. (17) to remove rotation error. We can then conclude that the remaining error can be attributed to other causes, provided that the fitted $|\Delta\theta| < 1.1°$.

B. Laboratory Validation

The calibration fitting procedure of Section 5 was implemented on a total of 14 replicated 26-position empty polarimeter measurements, where we refer to each replicated measurement as a "trial." The average fitted value for each LED wavelength across all 14 trials was then used during data reduction. Of critical importance are the generator and analyzer QWPs' retardances, which are depicted in Fig. 9(a), as well as the retarders' fast axis error, depicted in Fig. 9(b). Notable is that both QWPs have

Table 3. Measured Wave Plate Retardance Values (δ) and Estimated Errors (ϵ), in Degrees, at Each Nominal LED Wavelength λ_k in nm[a]

	λ_k								
P	**405**	**415**	**455**	**530**	**615**	**660**	**680**	**700**	**730**
k	1	2	3	4	5	6	7	8	9
$\Delta\lambda$ (nm)	14.8	13.8	18.8	34.6	19	20.2	20.4	18	26.2
λ_0 (nm)	411.4	417.9	447.3	521.7	628.5	657.0	683.8	698.3	722.8
PAR	13.5	67.6	98.2	13.2	147.0	290.7	50.8	12.3	20.9
δ_{HWP}	271.5	265.9	240.3	195.1	154.2	146.2	139.3	135.8	130.8
ϵ_{HWP}	±0.75	±0.60	±0.85	±3.15	±1.9	±1.15	±1.0	±0.85	±0.75
δ_{QWP}	163.1	160	144.5	117.6	93.6	88.9	86.1	85.6	80.5
ϵ_{QWP}	±1.7	±1.1	±0.65	±0.45	±0.3	±0.3	±0.25	±0.25	±0.25

[a]The LEDs' measured FWHM spectral bandwidths $\Delta\lambda$ and Gaussian-centered peak wavelengths λ_0 are also provided, along with the index k for each LED and its photosynthetically active radiation (PAR) value in $\mu\mathrm{mol}\cdot s^{-1}\cdot \mathrm{m}^{-2}$.

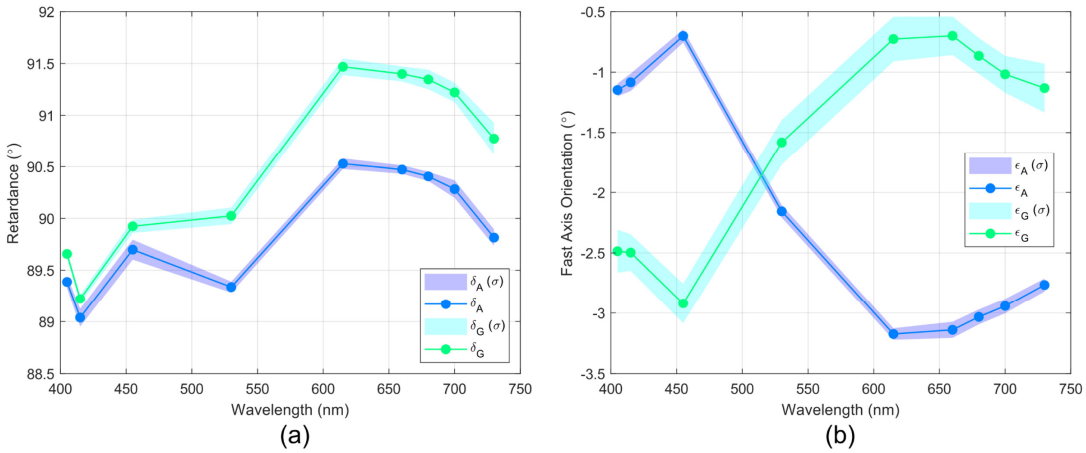

Fig. 9. Results of the fitting procedure depicting (a) fitted retardance and (b) fast axis orientation error versus wavelength. Error was calculated using the standard deviation across 14 trials.

values of $90° \pm 1.5°$ across the spectral passband. Finally, the standard deviation of each plot was calculated across the 14 trials.

Measurements were taken of the four film reference targets against each fiducial (two fiducials per film), in both their nominal and flipped orientations, yielding a total of 16 unique measurements. A separate measurement was also taken of the tilted fused silica glass plate, yielding a total of $L = 17$ reference target measurements. Both eight- and 26-position data were collected of each target, with $U = 4$ trials in each configuration. Thus, we collected and analyzed a total of 72 separate measurements in both the eight- and 26-position configurations. The mean absolute error, per Eq. (17), was first calculated for each reference element across all $K = 9$ wavelengths by

$$\alpha_{l,r} = \frac{1}{4K}\sum_{u=1}^{U}\sum_{k=1}^{K}\epsilon_{u,l,r}(\lambda_k), \tag{18}$$

where r is an integer spanning 1 to $R = 16$ for each of the Mueller matrix elements in $\epsilon_{u,l,r}(\lambda_k)$ from Eq. (17), defined as

$$\begin{bmatrix} m_{00} & m_{01} & m_{02} & m_{03} \\ m_{10} & m_{11} & m_{12} & m_{13} \\ m_{20} & m_{21} & m_{22} & m_{23} \\ m_{30} & m_{31} & m_{32} & m_{33} \end{bmatrix} = \begin{bmatrix} 1 & 2 & 3 & 4 \\ 5 & 6 & 7 & 8 \\ 9 & 10 & 11 & 12 \\ 13 & 14 & 15 & 16 \end{bmatrix}. \tag{19}$$

The results of Eq. (18) are depicted in Fig. 10 from the eight- and 26-position measurement configurations, calculated for each of the 16 polarization film reference targets. The amount of rotation $\Delta\theta$ needed to minimize rotational error per Eq. (17) is also provided in the figure. The empty polarimeter's error is also depicted in Fig. 11(a) alongside that of the tilted fused silica glass plate in Fig. 11(b). Finally, the error is represented in a box plot for each Mueller matrix element, calculated from all 16 reference polarizers and the tilted fused silica glass in Figs. 12(a) and 12(b) for the 26- and eight-measurement configurations, respectively. From these results, the average absolute value of the error, taken across all Mueller matrix elements, was calculated to be $(5.3 \pm 2.2) \times 10^{-3}$ for the 26-measurement configuration and $(7.1 \pm 3.1) \times 10^{-3}$ for the eight-measurement configuration.

Calculations were also performed to quantify error in each Mueller matrix element versus wavelength across all $U = 4$ trials and $L = 16$ films, as calculated by

$$\boldsymbol{\alpha}_r(\lambda_k) = \frac{1}{4L}\sum_{u=1}^{U}\sum_{l=1}^{L}\boldsymbol{\epsilon}_{u,l,r}(\lambda_k). \tag{20}$$

This absolute error and its associated standard deviation are depicted in Figs. 13(a) and 13(b) for the 26- and eight-position measurement configurations, respectively.

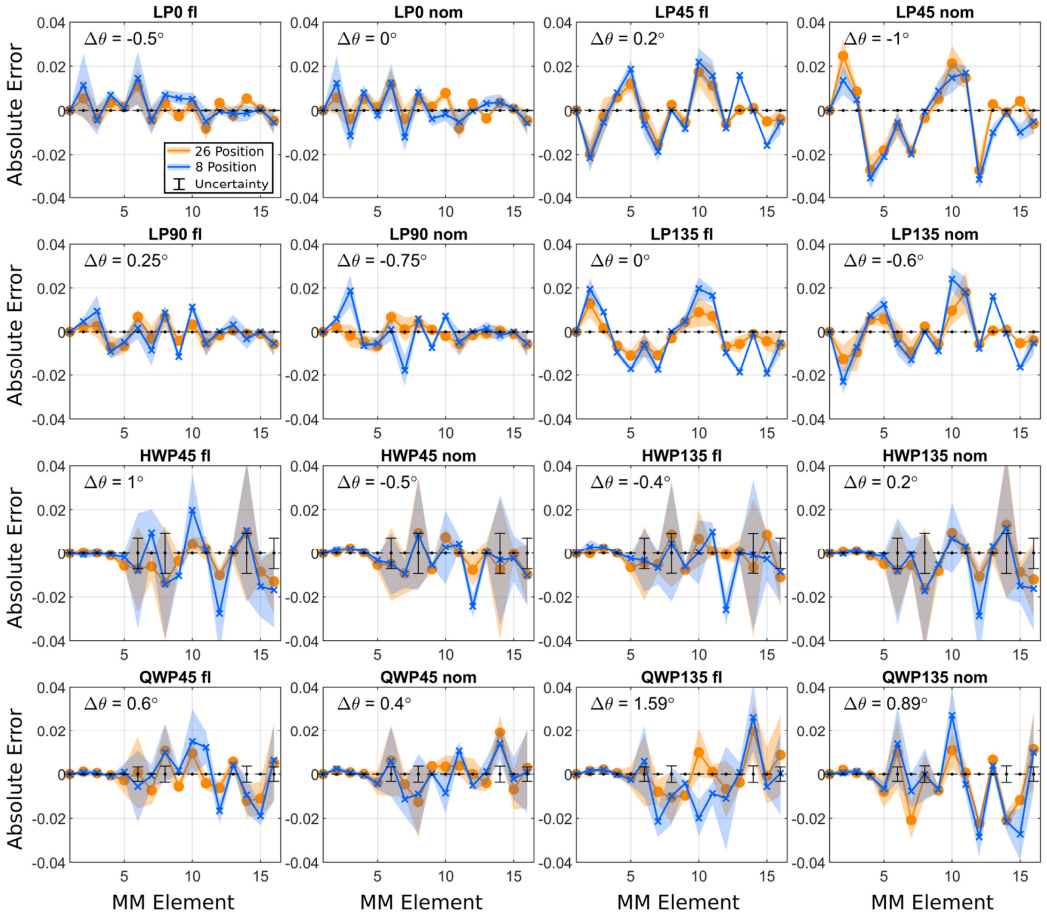

Fig. 10. Error residuals for each Mueller matrix element of the 16 calibration targets. Error bars represent uncertainty in the linear polarizer's extinction ratio of ±10% and in the QWP's or HWP's retardance, ϵ_{QWP} and ϵ_{HWP} per Table 3, respectively.

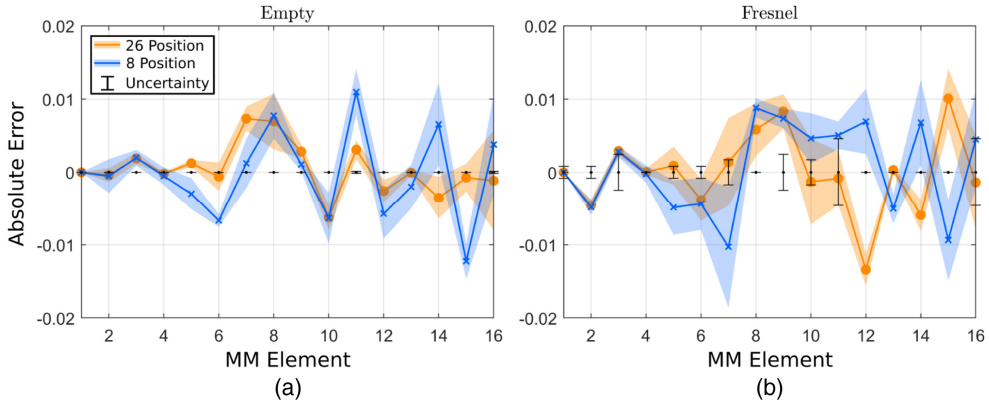

Fig. 11. Error residuals for the (a) empty polarimeter and (b) Fresnel reflections from a tilted fused silica glass window.

C. Outdoor Results

Data were collected using the sensor outdoors to establish a baseline in a *Z. Maize* hybrid to quantify how variable the Mueller matrix metrics are versus barrenness [40,41], leaf canopy location, and position on a single leaf. To establish this baseline, hybrid maize seeds (G90 sweet corn variety) were planted on 20 April 2022. On 24 June 2022 (65 days after planting) and 2 July 2022 (73 days after planting), the ears were physically removed from two of the G90 plants. Measurements were then taken with the polarimeter on 18 July 2022 (89 days after planting) at 7 PM local time (UTC -4). This established two treatments consisting of 16 days and 24 days of barrenness, along with one control. Due to its increased speed and higher throughput, all measurements used the eight-position (hybrid) configuration.

Measurements were taken in the field (Fig. S1) by removing the leaves, starting from the leaf closest to the tassel (leaf 1) and ending with the seventh leaf from the top. Generally, all three plants had leaves of equal maturity except the 24d barren leaf 1, which was unusable, and the 24d barren leaf 6, which had

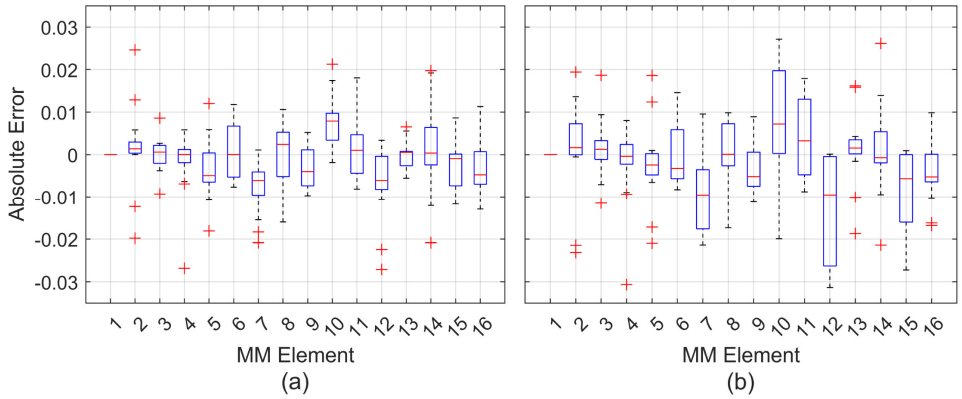

Fig. 12. Absolute error averaged over all 16 calibration targets and the Fresnel reflection sample.

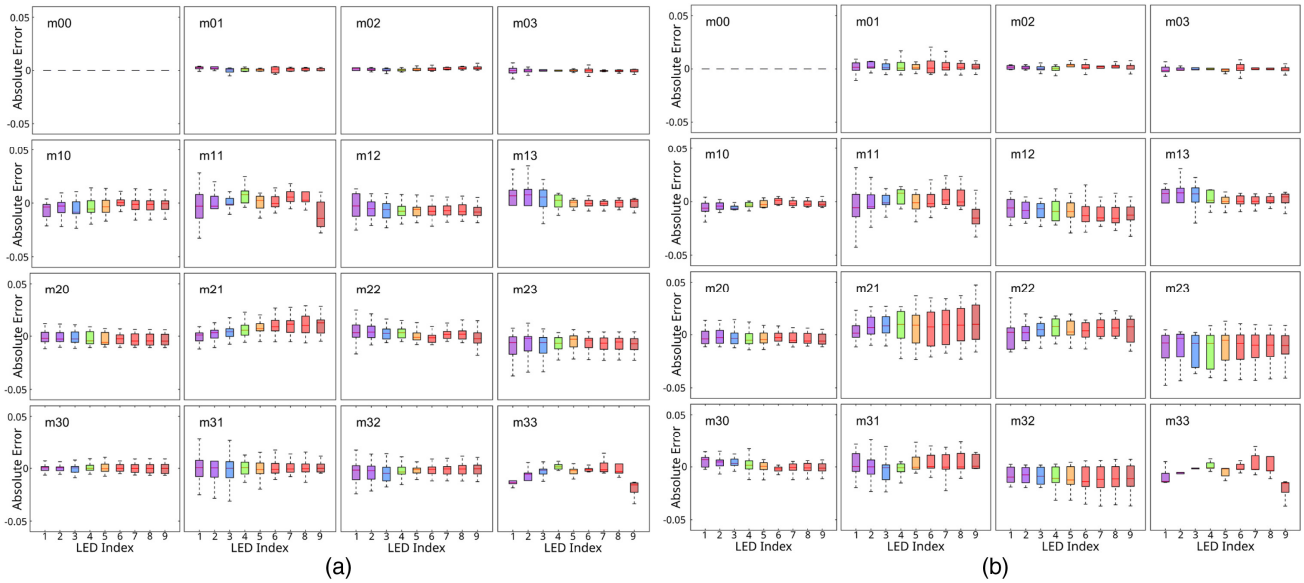

Fig. 13. Absolute error in each normalized Mueller matrix element (m_{01}/m_{00} to m_{33}/m_{00}) versus LED index for the (a) 26- and (b) eight-position measurement configurations.

been destroyed during ear removal. The imagery of each leaf and from each plant, alongside the Lu–Chipman decomposed retardance, diattenuation, and depolarization data [29,42], is presented in Supplement 1 Figs. S2–S7 for leaves 1–6, respectively. Additionally, Fig. S8 depicts only ear leaves that were measured from each plant, which represented leaf 7 for the control plant, leaf 6 for the 16d earless plant, and leaf 8 for the 24d earless plant. Measurements were taken along the length of each leaf where feasible. Exceptions included certain leaves on the 24d earless plant that were unusable or senesced. The retardance, diattenuation, and depolarization from each plant are summarized for three wavelengths ($\lambda = 450$ nm, 530 nm, and 680 nm) in Fig. 14(a). Values were calculated by spatially averaging 10 regions of interest (ROIs) across the sensor's FOV. Each ROI represented ± 30 pixels and was averaged along both the x and y axes.

7. DISCUSSION

From the validation experiments summarized in Section 6.B, we observed the expected nearly achromatic retardance from the BVO achromatic QWP. Additionally, it was observed that the fast axis orientation of the QWPs contains dispersion, as indicated in Fig. 9(b) and is common with achromatic wave plates of this type [43]. There was also an inverted relationship in the fast axis orientations versus wavelength between the analyzing and generating QWPs in Fig. 9(b), which was caused by flipping the orientation of one QWP relative to the other (e.g., a five-layer QWP with light traversing layers 1 to 5 versus layers 5 to 1). This is not expected to have significantly impacted the polarimeter's performance since it can be accounted for during data reduction.

Regarding the validation experiments, it was noted that the reference LPs' rotational errors were less than 1°, as per the measurement accuracy of Table 2. Similarly, for wave plate film reference targets, the absolute difference in $\Delta\theta$, calculated between the nominal and flipped orientations for all films, is generally less than 1.1° as anticipated from Section 6.A. One exception occurred with the QWP at 135°, measured in its flipped orientation, which had $\Delta\theta = 1.59°$. This may be an outlier caused by the positional repeatability, despite exceeding the 2σ error that was anticipated from Section 6.A.

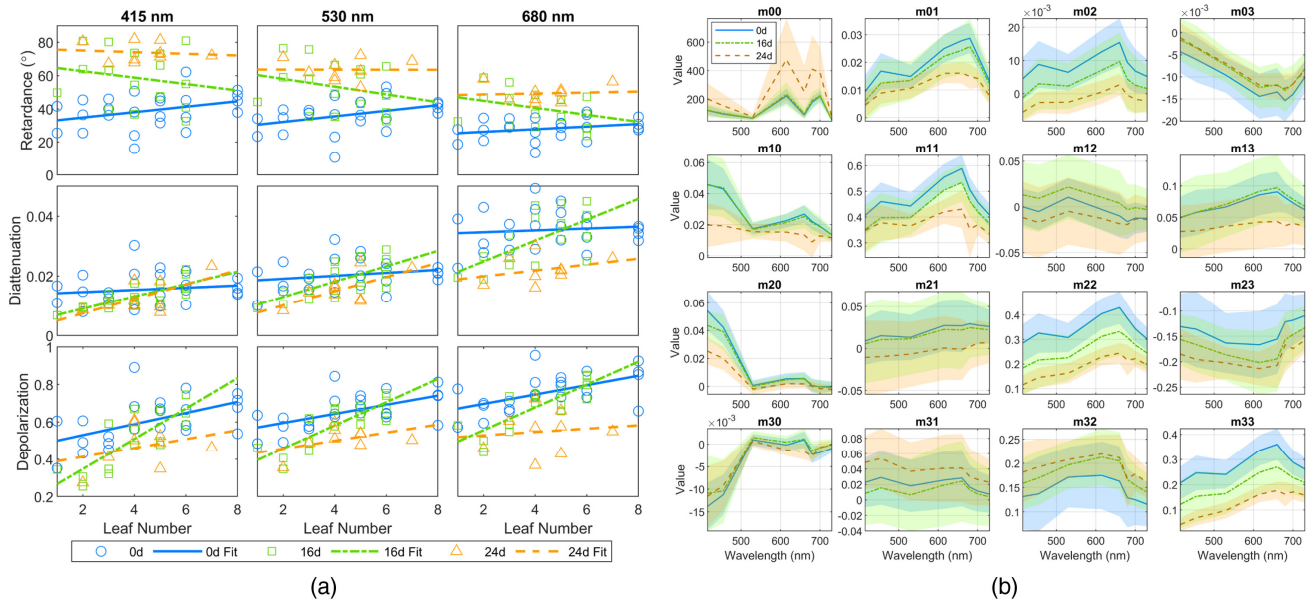

Fig. 14. (a) Spatially averaged retardance (top row), diattenuation (middle row), and depolarization (bottom row) versus leaf number at wavelengths of 415 nm (first column), 530 nm (middle column), and 680 nm (last column). Results are shown for the 0d control plant (blue circle), 16d earless plant (green square), and 24d earless plant (orange triangle). A linear model was also fit to the 0d control plant (solid blue line), 16d barren plant (dashed-dotted green line), and 24d barren plant (dashed orange line). (b) Variation in Mueller matrix elements versus wavelength. Control (magenta solid line), 16d earless (blue solid line), and 24d earless plant (cyan solid line) with associated shaded regions denoting $\pm 1\sigma$, as calculated across all ROIs.

Finally, it should be noted that the same value of $\Delta\theta$ was used to compensate for all four trials before calculating the error.

Absolute error calculated for each Mueller matrix element over all wavelengths λ_k, per Fig. 12, generally represented values spanning ± 0.01 peak-to-peak for the 26-measurement configuration and ± 0.026 peak-to-peak for the eight-measurement configuration, with reference to the errors' first and third quartiles. As highlighted in the results, the absolute value of the absolute error, taken across all 15 normalized Mueller matrix elements, was also lower for the 26-measurement configuration versus the eight-measurement configuration, with values of $(5.3 \pm 2.2) \times 10^{-3}$ and $(7.1 \pm 3.1) \times 10^{-3}$, respectively. As indicated in Fig. 12, error was also more similar across all Mueller matrix elements in the 26-measurement configuration compared to the eight-measurement configuration, in which Mueller matrix elements, in order from highest to lowest absolute error, included $r = 12, 10, 11, 7$, and 15, corresponding to m_{23}, m_{21}, m_{22}, m_{12}, and m_{32}, respectively. Such behavior is not unexpected, since operating the polarimeter in a more complex channeled mode (e.g., modulating information in both time and space versus only time or only space) represents a complex tradespace with respect to noise within each Mueller matrix element [22,44,45]. Future work will be aimed at applying these emerging optimization techniques to, for instance, minimize noise in m_{23} to investigate its impact on other elements.

The absolute error, calculated for each Mueller matrix element at each wavelength in Fig. 13, follows trends similar to those observed when error was calculated across all wavelengths. For instance, in the eight-position data of Fig. 13(b), Mueller matrix elements m_{23}, m_{21}, m_{22}, m_{12}, and m_{32} generally demonstrated worse error than the elements in the first row or first columns. Conversely, in the 26-position data of Fig. 13(a), error among all elements is generally similar. Error at the shortest and longest wavelengths also appears to be worse than in mid-band wavelengths, for instance, m_{33} at 730 nm or m_{11} at 405 nm. This is likely impacted by the dichroic LP film used in the instrument's generating polarizer, in that the extinction ratio decreases at these wavelengths. Finally, some trends in the error, such as the gradual increase in error observed in m_{21} versus increasing wavelength for the 26-measurement configuration of Fig. 13(a), may be caused by residual uncertainty in the reference samples. While reference targets of alternate designs, such as a Fresnel rhomb, right angle prism, or birefringent polarizer (e.g., a Glan–Thompson polarizer) would have offered a more ideal and achromatic Mueller matrix, the approach used here has established the performance limits of the polarimeter within the uncertainty of the elements that were used. This is highlighted in Fig. 10, in that the error bars associated with the elements' uncertainty, per Table 3, are smaller than the polarimeter's measured uncertainty. Notable is that the elements containing the largest error are also associated with larger underlying uncertainty, especially with the HWP measurements. Overall, the higher retardance of the HWP contributes to greater uncertainty versus wavelength across the spectrum of the LED. This implies that the spectral bandwidth is also an intrinsically limiting factor, as highlighted in other studies when comparing polychromatic versus monochromatic polarimetric measurements [46]. One interesting area of future work will also be to study the application of maximum likelihood techniques for calibration, which removes the need for calibrating using wave plates such as these [31].

Finally, with respect to our *Z. maize* baselines, we were able to observe several trends in the data that correlated with barrenness in the literature. These included the following.

1. As described by Crafts-Brander *et al.* per Ref. [47], the visual signs of leaf senescence, associated with barren plants, had a tendency to progress from the top of the canopy down. Conversely, leaf senescence associated with normally maturing eared plants progressed bottom-up. While these observations were made for P3382 and B73 × Mo17 maize hybrids, our G90 hybrid progressed in a similar fashion with respect to its visual appearance. Notable is that a general trend, at 16d after ear removal, was observed in the polarization metrics versus leaf position in Fig. 14(a), in that the slope of the retardance and depolarization metrics at all wavelengths, as well as at 680 nm, changed for the 16d plant compared to the 0d and 24d plants. Additionally, the general change in this trend versus leaf position is observable before clear visual symptoms were evident as per Figs. S2–S8, in either the red, green, and blue imagery collected by the sensor or from the cellphone images captured of the leaves just prior to the measurements. This is also despite highly similar S_0 trends versus wavelength observed in $m00$ of Fig. 14(b). Finally, a general top-to-bottom canopy trend may be observed even in control plants, based on the fact that upper-canopy leaves produce more nonstructural carbohydrates than mid- or lower-canopy leaves [48,49]. However, whether the observed trends in the data are caused by carbohydrate content, chlorophyll concentration, or leaf thickness is a topic of future study.
2. Barrenness also created an offset in the depolarization and retardance observed at 415 and 530 nm, as well as the diattenuation at 680 nm, compared to the 0d control per Fig. 14(a). It is expected that this could be caused by not only a reduction of chlorophyll, but also an over-accumulation of starch and sugar in the leaf tissue. Although not observed with a full Mueller matrix polarimeter, it is thought that polarization metrics associated with starch accumulation creates a polarization rotation in the light reflected from plants with high starch presence [19]. Photosynthesis is negatively impacted by ear removal, leading to an over-accumulation of starch and sugar in the different tissues of the maize plant. This is especially true for the stalk, which has higher sugar content in barren plants (17%) versus normal controls (8%) [40]. However, leaves do increase appreciably in sugar content in barren plants (5–7 g/plant) versus normal controls (3 g/plant), as well as in starch (1.5–2.5 g/plant barren versus 0.5 g/plant control) for some hybrids [47].

Improved ground truth data provided by techniques such as NMR spectroscopy will be used in the future to determine which specific metabolites (e.g., sugar, starch, chlorophyll, etc.) these signatures best correlate with.

8. CONCLUSION

In this paper, we have demonstrated a portable imaging Mueller matrix polarimeter with high radiometric throughput and sample radiance. This enables reduced measurement times (34 s per measurement sequence) for capturing transmission Mueller matrices through highly diffuse or absorbing plants, at nine wavelengths, in field conditions. Ultimately, using the LEDs' intrinsic spectra enables fast electrical switching between the various wavelengths while offering speckle-free illumination at high power densities, while the piezoelectric motors enable rapid rotation of the polarization elements between states, and the use of a polarization microgrid camera offers the ability to further compress the measurement time compared to a more conventional measurement sequence. The mean absolute values of the absolute errors taken over all wavelengths for the polarimeter were demonstrated to be $(5.3 \pm 2.2) \times 10^{-3}$ and $(7.1 \pm 3.1) \times 10^{-3}$ for the 26- and eight-measurement configurations, respectively. Future work will focus on collecting and publishing a database of spectral Mueller matrices with associated chemical and metabolic ground truth, using the setup to test emerging calibration and optimization techniques, and assessing MMP for applications within high throughput plant phenotyping pipelines.

Funding. Division of Electrical, Communications and Cyber Systems (1809753); National Institute of Food and Agriculture (2020-67021-31961).

Disclosures. The authors declare no conflicts of interest.

Data availability. Data underlying the results presented in this paper are not publicly available at this time but may be obtained from the authors upon reasonable request.

Supplemental document. See Supplement 1 for supporting content.

REFERENCES

1. A. Le Gratiet, A. Mohebi, F. Callegari, P. Bianchini, and A. Diaspro, "Review on complete Mueller matrix optical scanning microscopy imaging," Appl. Sci.—Basel **11**, 1632 (2021).
2. J. Qi and D. S. Elson, "Mueller polarimetric imaging for surgical and diagnostic applications: a review," J. Biophoton. **10**, 950–982 (2017).
3. A. Pierangelo, A. Benali, M.-R. Antonelli, T. Novikova, P. Validire, B. Gayet, and A. De Martino, "Ex-vivo characterization of human colon cancer by Mueller polarimetric imaging," Opt. Express **19**, 1582–1593 (2011).
4. T. Liu, T. Sun, H. He, S. Liu, Y. Dong, J. Wu, and H. Ma, "Comparative study of the imaging contrasts of Mueller matrix derived parameters between transmission and backscattering polarimetry," Biomed. Opt. Express **9**, 4413–4428 (2018).
5. D. A. Luo, E. T. Barraza, and M. W. Kudenov, "Mueller matrix polarimetry on plasma sprayed thermal barrier coatings for porosity measurement," Appl. Opt. **56**, 9770–9778 (2017).
6. D. Necas, I. Ohlidal, D. Franta, M. Ohlidal, V. Cudek, and J. Vodak, "Measurement of thickness distribution, optical constants, and roughness parameters of rough nonuniform ZnSe thin films," Appl. Opt. **53**, 5606–5614 (2014).
7. J. E. Wolfe and R. A. Chipman, "Polarimetric characterization of liquid-crystal-on-silicon panels," Appl. Opt. **45**, 1688–1703 (2006).
8. S. Yuanxing, Y. Yue, H. Honghui, L. Shaoxiong, and M. Hui, "Mueller matrix polarimetry: a label-free, quantitative optical method for clinical diagnosis," Chin. J. Lasers/Zhongguo Jiguang **47**, 0207001 (2020).
9. D. N. Ignatenko, A. V. Shkirin, Y. P. Lobachevsky, and S. V. Gudkov, "Applications of Mueller matrix polarimetry to biological and agricultural diagnostics: a review," Appl. Sci. **12**, 5258 (2022).
10. C. H. L. Patty, D. A. Luo, F. Snik, F. Ariese, W. J. Buma, I. L. ten Kate, R. J. M. van Spanning, W. B. Sparks, T. A. Germer, G. Garab, and M. W. Kudenov, "Imaging linear and circular polarization features in leaves with complete Mueller matrix polarimetry," Biochim. Biophys. Acta—Gen. Subj. **1862**, 1350–1363 (2018).
11. B. A. Bugami, Y. Su, C. Rodríguez, A. Lizana, J. Campos, M. Durfort, R. Ossikovski, and E. Garcia-Caurel, "Characterization of vine, vitis vinifera, leaves by Mueller polarimetric microscopy," Thin Solid Films **764**, 139594 (2022).

12. S. N. Savenkov, R. S. Muttiah, and Y. A. Oberemok, "Transmitted and reflected scattering matrices from an English oak leaf," Appl. Opt. **42**, 4955–4962 (2003).
13. C. Xiao-feng, Y. Ke-qiang, Z. Yan-ru, and Z. Hai-hui, "Current status of high-throughput plant phenotyping for abiotic stress by imaging spectroscopy: A review," Spectrosc. Spectral Anal. **40**, 3365–3372 (2020).
14. C. Farber, M. Mahnke, L. Sanchez, and D. Kurouski, "Advanced spectroscopic techniques for plant disease diagnostics. A review," TRAC Trends Anal. Chem. **118**, 43–49 (2019).
15. N. R. Baker, "Chlorophyll fluorescence: a probe of photosynthesis in vivo," Annu. Rev. Plant Biol. **59**, 89–113 (2008).
16. K. Maxwell and G. N. Johnson, "Chlorophyll fluorescence—a practical guide," J. Exp. Bot. **51**, 659–668 (2000).
17. C. Rodriguez, E. Garcia-Caurel, T. Garnatje, M. Serra i Ribas, J. Luque, J. Campos, and A. Lizana, "Polarimetric observables for the enhanced visualization of plant diseases," Sci. Rep. **12**, 14743 (2022).
18. A. V. Eeckhout, E. Garcia-Caurel, T. Garnatje, M. Durfort, J. C. Escalera, J. Vidal, J. J. Gil, J. Campos, and A. Lizana, "Depolarizing metrics for plant samples imaging," PLOS ONE **14**, e0213909 (2019).
19. A. Pourreza, W. S. Lee, E. Czarnecka, L. Verner, and W. Gurley, "Feasibility of using the optical sensing techniques for early detection of huanglongbing in citrus seedlings," Robotics - Basel **6**, 11 (2017).
20. M. W. Kudenov, D. Krafft, C. G. Scarboro, C. J. Doherty, and P. Balint-Kurti, "Fieldable Mueller matrix imaging spectropolarimeter using a hybrid spatial and temporal modulation scheme," Proc. SPIE **11833**, 118330E (2021).
21. D. Gottlieb and O. Arteaga, "Mueller matrix imaging with a polarization camera: application to microscopy," Opt. Express **29**, 34723–34734 (2021).
22. A. S. Alenin and J. S. Tyo, "Generalized channeled polarimetry," J. Opt. Soc. Am. A **31**, 1013–1022 (2014).
23. J. Song, I. J. Vaughn, A. S. Alenin, and J. S. Tyo, "Imaging dynamic scenes with a spatio-temporally channeled polarimeter," Opt. Express **27**, 28423–28436 (2019).
24. K. Oka and T. Kato, "Spectroscopic polarimetry with a channeled spectrum," Opt. Lett. **24**, 1475–1477 (1999).
25. K. H. Nordsieck, "A simple polarimetric system for the lick observatory image-tube scanner," Publ. Astron. Soc. Pac. **86**, 324–329 (1974).
26. F. Snik, T. Karalidi, and C. U. Keller, "Spectral modulation for full linear polarimetry," Appl. Opt. **48**, 1337–1346 (2009).
27. W. Sparks, T. A. Germer, J. W. MacKenty, and F. Snik, "Compact and robust method for full Stokes spectropolarimetry," Appl. Opt. **51**, 5495–5511 (2012).
28. M. W. Kudenov, N. A. Hagen, E. L. Dereniak, and G. R. Gerhart, "Fourier transform channeled spectropolarimetry in the MWIR," Opt. Express **15**, 12792–12805 (2007).
29. R. A. Chipman, W.-S. T. Lam, and G. Young, *Polarized Light and Optical Systems*, 1st ed. (CRC Press, 2018).
30. H. Hu, E. Garcia-Caurel, G. Anna, and F. Goudail, "Maximum likelihood method for calibration of Mueller polarimeters in reflection configuration," Appl. Opt. **52**, 6350–6358 (2013).
31. H. Hu, E. Garcia-Caurel, G. Anna, and F. Goudail, "Simplified calibration procedure for Mueller polarimeter in transmission configuration," Opt. Lett. **39**, 418–421 (2014).
32. D. H. Goldstein, *Polarized Light* (CRC Press, 2011).
33. J. S. Tyo, D. L. Goldstein, D. B. Chenault, and J. A. Shaw, "Review of passive imaging polarimetry for remote sensing applications," Appl. Opt. **45**, 5453–5469 (2006).
34. F. Goudail, "Equalized estimation of Stokes parameters in the presence of Poisson noise for any number of polarization analysis states," Opt. Lett. **41**, 5772–5775 (2016).
35. M. N. Akram and X. Chen, "Speckle reduction methods in laser-based picture projectors," Opt. Rev. **23**, 108–120 (2015).
36. D. S. Mehta, D. N. Naik, R. K. Singh, and M. Takeda, "Laser speckle reduction by multimode optical fiber bundle with combined temporal, spatial, and angular diversity," Appl. Opt. **51**, 1894–1904 (2012).
37. A.-B. Mahler, P. K. Smith, and R. A. Chipman, "Low polarization optical system design," Proc. SPIE **6682**, 260–269 (2007).
38. J. D'Errico, "fminsearchbnd, fminsearchcon," (2012).
39. I. H. Malitson, "Interspecimen comparison of the refractive index of fused silica," J. Opt. Soc. Am. **55**, 1205–1209 (1965).
40. D. N. Moss, "Photosynthesis and barrenness," Crop Sci. **2**, 366–367 (1962).
41. S. J. Crafts-Brandner and C. G. Poneleit, "Effect of ear removal on CO_2 exchange and activities of ribulose bisphosphate carboxylase/oxygenase and phosphoenolpyruvate carboxylase of maize hybrids and inbred lines," Plant Physiol. **84**, 261–265 (1987).
42. S.-Y. Lu and R. A. Chipman, "Interpretation of Mueller matrices based on polar decomposition," J. Opt. Soc. Am. A **13**, 1106–1113 (1996).
43. D. Clarke, "Interference effects in Pancharatnam wave plates," J. Opt. A **6**, 1047 (2004).
44. A. S. Alenin, I. J. Vaughn, and J. S. Tyo, "Optimal bandwidth and systematic error of full-stokes micropolarizer arrays," Appl. Opt. **57**, 2327–2336 (2018).
45. I. J. Vaughn, A. S. Alenin, and J. S. Tyo, "Channeled spatio-temporal Stokes polarimeters," Opt. Lett. **43**, 2768–2771 (2018).
46. M. W. Kudenov, J. L. Pezzaniti, and G. R. Gerhart, "Microbolometer-infrared imaging Stokes polarimeter," Opt. Eng. **48**, 063201 (2009).
47. S. J. Crafts-Brandner, F. E. Below, J. E. Harper, and R. H. Hageman, "Differential senescence of maize hybrids following ear removal 1: I. Whole plant," Plant Physiol. **74**, 360–367 (1984).
48. S. Moustafa, "Physiological characters in maize (Zea. Mays L.) and their relationship to stalk rot," Ph.D. thesis (Iowa State University, 1979).
49. J. C. S. Allison and D. J. Watson, "The production and distribution of dry matter in maize after flowering," Ann. Bot. **30**, 365–381 (1966).